ARTICLE   OPEN

Check for updates

Local decorin delivery via hyaluronic acid microrods improves cardiac performance, ventricular remodeling after myocardial infarction

Priya Mohindra [1,2], Justin X. Zhong [1,2], Qizhi Fang[3], Darnell L. Cuylear [2,4], Cindy Huynh[2,5], Huiliang Qiu[3], Dongwei Gao[3], Bhushan N. Kharbikar [2], Xiao Huang[2], Matthew L. Springer[3], Randall J. Lee[1,3,6] and Tejal A. Desai [1,2,6,7 ✉]

Heart failure (HF) remains a global public health burden and often results following myocardial infarction (MI). Following injury, cardiac fibrosis forms in the myocardium which greatly hinders cellular function, survival, and recruitment, thus severely limits tissue regeneration. Here, we leverage biophysical microstructural cues made of hyaluronic acid (HA) loaded with the anti-fibrotic proteoglycan decorin to more robustly attenuate cardiac fibrosis after acute myocardial injury. Microrods showed decorin incorporation throughout the entirety of the hydrogel structures and exhibited first-order release kinetics in vitro. Intramyocardial injections of saline ($n = 5$), microrods ($n = 7$), decorin microrods ($n = 10$), and free decorin ($n = 4$) were performed in male rat models of ischemia-reperfusion MI to evaluate therapeutic effects on cardiac remodeling and function. Echocardiographic analysis demonstrated that rats treated with decorin microrods ($5.21\% \pm 4.29\%$) exhibited significantly increased change in ejection fraction (EF) at 8 weeks post-MI compared to rats treated with saline ($-4.18\% \pm 2.78\%$, $p < 0.001$) and free decorin ($-3.42\% \pm 1.86\%$, $p < 0.01$). Trends in reduced end diastolic volume were also identified in decorin microrod-treated groups compared to those treated with saline, microrods, and free decorin, indicating favorable ventricular remodeling. Quantitative analysis of histology and immunofluorescence staining showed that treatment with decorin microrods reduced cardiac fibrosis ($p < 0.05$) and cardiomyocyte hypertrophy ($p < 0.05$) at 8 weeks post-MI compared to saline control. Together, this work aims to contribute important knowledge to guide rationally designed biomaterial development that may be used to successfully treat cardiovascular diseases.

npj Regenerative Medicine (2023)8:60 ; https://doi.org/10.1038/s41536-023-00336-w

INTRODUCTION

Heart failure (HF) affects ~6 million Americans, and the prevalence is projected to increase 46% from 2012 to 2030[1]. The prognosis for HF is poor, with an estimated mortality rate of ~50% within 5 years of the diagnosis[1]. Myocardial infarction (MI) from coronary artery disease is the leading cause of HF and despite advances in the management of MI, subsequent pathologic remodeling of ischemic myocardium with fibrotic scar tissue and aneurysmal degeneration leads to HF and death[2]. Therefore, therapies that can prevent scar tissue formation, increase cell survival, and promote contractile tissue regeneration need to be identified to treat this growing patient population in the wake of increasing rates of obesity and heart disease[1]. To date, cellular therapies have had limited success in promoting long-term cardiovascular repair[3,4] and no delivery system for an effective pharmacotherapy exists. Moreover, current treatment of fibrosis involves systemic inhibition of cytokines and chemokines which leads to many adverse side effects for patients[5,6].

In recent years, there has been growing interest in targeting pathways that lead to altered cardiovascular cell phenotypes and microenvironments after injury to reduce maladaptive repair and promote functional recovery. As most of these cell types are mechanosensitive and rely on micro- and nanoscale cues from the extracellular matrix (ECM) to dictate homeostatic function, it is possible to harness these interactions through biomaterials with similar size scale biophysical cues to elicit more native cell phenotypes, thereby mitigating cardiovascular disease progression and enhancing regenerative potential[7]. Fibroblasts represent the largest percentage of cells in the heart and coordinate numerous functions including ECM turnover, cell-cell signaling, and cytokine and growth factor secretion[8]. After MI, fibroblasts transform into a highly contractile, activated myofibroblast phenotype, which functions to stabilize the injury site by increasing ECM deposition to preserve the integrity of the myocardial wall and maintain the pressure generating ability of the heart[9]. While this compensatory process is initially beneficial, problems arise when pro-fibrotic signals such as TGF-β1 persist, leading to continual deposition of stiff scar tissue which ultimately impairs contractility and perfusion within in the heart[9].

We have previously demonstrated the ability to modulate fibroblast morphology and function using polymeric microstructural cues to achieve less fibrotic phenotypes, which could have potential significance in HF therapy[10–13]. Recent work showed that in vitro treatment with polymeric microrods ($15 \times 15 \times 100$ μm) decreased fibroblast proliferation and that microrod injections in preclinical rodent models of HF cause reductions in scar tissue and improvements in cardiac function by influencing the cardiac microenvironment[12,13]. Benefits of using hydrogel microstructure strategies with mechanobiological mechanisms of action as therapeutic approaches include being injectable, cell-free, and

[1]UC Berkeley-UCSF Graduate Program in Bioengineering, San Francisco, CA, USA. [2]Department of Bioengineering and Therapeutic Sciences, University of California, San Francisco, San Francisco, CA, USA. [3]Division of Cardiology, University of California, San Francisco, San Francisco, CA, USA. [4]Graduate Program in Graduate Program in Oral and Craniofacial Sciences, School of Dentistry, University of California, San Francisco, San Francisco, CA, USA. [5]Division of Vascular and Endovascular Surgery, Department of Surgery, Brigham and Women's Hospital, Harvard Medical School, Boston, MA, USA. [6]Department of Bioengineering, University of California, Berkeley, Berkeley, CA, USA. [7]School of Engineering, Brown University, Providence, RI, USA. ✉email: Tejal_Desai@brown.edu

npj

highly tunable in terms of geometry, stiffness, and material. Further, as their therapeutic effects are restricted based on proximity, concerns related to systemic side effects are avoided. Microrod hydrogels also allows for combination therapies with the ability to load and release various therapeutic factors from the microstructures[14,15]. The ability to devise more potent, multifaceted therapies can have tremendous implications on myocardial regeneration after MI by addressing multiple pathological processes.

Reperfusion strategies are a key component in the management of acute MI but can lead to ischemia reperfusion injury (IRI), which is widely characterized by oxidative stress, inflammation, intracellular Ca^{2+} overload, fibrosis, and endothelial dysfunction[16–18]. Although the exact mechanisms of IRI remain unknown, targeting oxidative damage and subsequent fibrotic response that occurs after myocardial injury and reperfusion is critical to cardiac recovery after MI[19–26]. Several naturally occurring biological macromolecules within the body possess unique characteristics that may enhance intrinsic wound healing functions after injury. Small leucine rich proteoglycans (SLRPs) are ubiquitous ECM components involved in structural organization and are known regulators of collagen fibril assembly[27]. Decorin, a class I SLRP, has been shown to have both anti-fibrotic and antioxidant properties. It has been reported to sequester the profibrotic cytokine TGF-β with high affinity and modulate collagen fibrillogenesis[28–34]. Preclinical studies have also demonstrated a therapeutic role of decorin in mitigating fibrosis in various in vivo models of ischemic injury[35–37] and in vitro fibrosis models[38–40]. Further, it has been reported that there is a protective role of decorin after traumatic injury in vivo which is linked to oxidative stress response[35,41]. In cell studies with high glucose and oxygen/glucose-deprived environments, protective effects of decorin center on involvement in apoptosis and oxidative stress pathways[42,43]. Therefore, there may exist an important role for decorin in early response therapies for cardiovascular injury.

Hence, our approach in this study is to introduce bioactive, decorin-loaded hyaluronic-acid (HA) microstructural cues into the post-infarct microenvironment to regulate pathological cell responses and transform the wound healing microenvironment by providing discrete micromechanical and biochemical cues. We demonstrate the impact of decorin microrods on cardiac function, ventricular remodeling, fibrosis, hypertrophy, and vascularization post-MI.

RESULTS

Decorin treatment reduces myofibroblast-like gene expression and inhibits collagen fibrillogenesis

To confirm anti-fibrotic biologic effects of decorin, NIH 3T3 fibroblasts were stimulated with 10 ng/mL TGF-β1 and cultured in the presence or absence of 10 µg/mL decorin. Relative gene expression results from RT-qPCR using primers specified in Supplementary Table 1 indicate stark reductions in ACTA2 ($p < 0.0001$), COL1A2 ($p < 0.01$), COL3A1 ($p < 0.001$), and MMP2 ($p < 0.05$) expression in decorin-treated samples compared to control (Supplementary Fig. 1). These results demonstrate decorin's ability to sequester TGF-β1 and prevent activation of its downstream signaling pathways that result in myofibroblast-like phenotypes in fibroblasts.

Turbidity was used to assess the degree of collagen fibrillogenesis. A broad range of decorin concentrations (2.5–40 µg/mL) were used to assess dose-dependent effects of decorin on collagen fiber formation. It is evident that fibril formation kinetics are dependent on decorin concentration, and while all doses of decorin tested significantly inhibited fibrillogenesis, the highest concentration of 40 µg/mL yielded the greatest impact at the 120 min. timepoint (Supplementary Fig. 2, $p < 0.01$).

Release of decorin from microrods

Next, we examined the loading and in vitro release dynamics of decorin from microrods. Decorin was loaded into microrods to achieve a more potent anti-fibrotic strategy that leveraged biophysical regulation of microstructures and the ability of decorin to sequester TGF-β1 in the post-infarct environment. Microrods were fabricated as previously described and loading according the scheme in Fig. 1 [13]. Morphological characteristics including size and shape of the microrods remained comparable before and after loading (Fig. 2a) and decorin microrods exhibited a loading efficiency of 80.3% (Supplementary Fig. 3). Release kinetics were assessed in PBS solution using aliquots of 50,000 microrods containing ~12 µg of decorin. Within the first 10 h, decorin exhibited burst release from the microrods with more than 5.7 µg being released into solution. Following this burst release, decorin release exhibits a plateau in release from hours 24 to 168 (Fig. 2b, c). Overall, the total hourly amount of eluted decorin decreased with time indicating concentration dependent (first-order) release kinetics from the decorin microrods.

Effect of decorin microrods in ischemia-reperfusion myocardial infarction in vivo models

From three independent studies, decorin loading was calculated to be ~10.7 µg of decorin per 50,000 microrods as measured via protein quantitation (Supplementary Fig. 3). A rodent model of ischemia-reperfusion MI was utilized to generate a cardiac fibrosis model. All treatments—saline, microrods, decorin microrods, or free decorin were delivered into the infarct via ultrasound-guided, intramyocardial injection. For subsequent animal studies, we chose to use the higher end of observed loading (~12 µg per 50,000 microrods) as the injection dose for the free decorin treatment group that served as a positive control (Table 1).

Microrod and decorin microrod treatments were shown to result in significant improvements in cardiac function when compared to saline and free decorin treatments (Fig. 3). When comparing baseline EF to EF at 8 weeks post-MI in Fig. 3a and Supplementary Table 2, while saline-treated animals experienced a decline in function ($p = 0.07$), microrod-treated animals did not experience a decline, and decorin microrod-treated animals exhibited a significant increase in EF ($p < 0.001$). Change in EF was assessed by taking the difference in EF measured at Day 3–4 post-MI and at 8 weeks post-MI (Fig. 3b, Supplementary Table 3). Rats treated with microrods (2.12% ± 4.35%) or decorin microrods (5.21% ± 4.29%) exhibited better change in EF at 8 weeks post-MI than rats treated with saline (−4.18% ± 2.78%) or free decorin (−3.42% ± 1.86%). Since decorin microrods performed better than microrods and free decorin, this suggests that the ability to locally retain decorin at the infarct site through the use of the microstructures was crucial to improving the efficacy of the microrod strategy. Rats treated with decorin microrods demonstrated a significantly better change in EF at 8 weeks post-MI compared to both saline and free decorin (Fig. 3b, $p < 0.001$ and $p < 0.01$, respectively). Trends in improved EF for the decorin microrod-treated group compared to saline and free decorin are also evident after 8 weeks (Supplementary Fig. 4, Supplementary Table 4; $p = 0.09$, $p < 0.01$, respectively). Ventricular remodeling was also improved in rats treated with decorin microrods as evidenced by significant reduction in ESV (Fig. 3c, Supplementary Table 5; $p < 0.05$, $p < 0.05$, $p < 0.001$, respectively) and importantly EDV compared to rats treated with saline, microrods, and free decorin (Fig. 3d, Supplementary Table 5; $p = 0.05$, $p < 0.01$, $p < 0.01$, respectively). Treatments with microrods and decorin microrods led to a better change in SV than treatments with either saline or free decorin after 8 weeks post-MI. Microrod-treated animals had significantly higher changes in SV compared to saline and free decorin groups (Fig. 3e, Table S3; $p < 0.05$ and $p < 0.01$, respectively) while decorin microrods showcased a
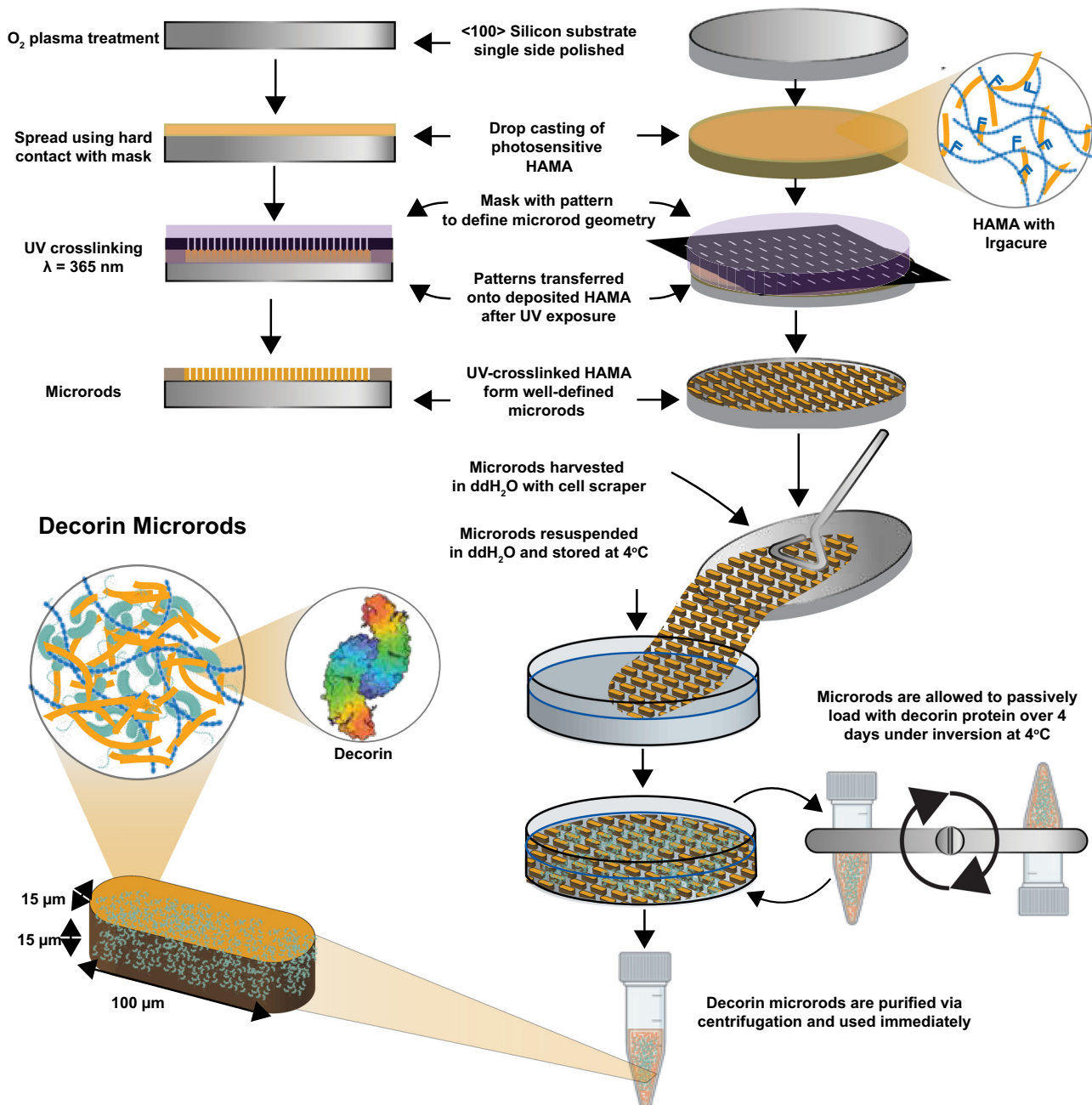
Fig. 1 Microrod fabrication scheme and loading with decorin. HA was first modified with a photosensitive handle to generate hyaluronic acid methacrylate (HAMA) polymer that is amenable to crosslinking via exposure to UV light in the presence of the photoinitiator 2-hydroxy-4′-(2-hydroxyethoxy)-2-methylpropiophenone (Irgacure). HAMA was deposited onto an oxygen plasma- or piranha-treated wafer and exposed to UV light through a photomask patterned with fixed rectangular geometries of 15 μm width by 100 μm length. After exposure, the polymer film was then developed in water to isolate the crosslinked microrods. Microrods were loaded with decorin via incubation with inversion at 4 °C over 4 days and then subsequently purified via centrifugation.

trend towards increased change in SV when compared to both vehicle and free decorin (Fig. 3e, Supplementary Table 3; $p = 0.18$, $p = 0.06$, respectively).

Histological evaluation of each treatment group was performed using H&E and Sirius red to assess LV wall thickness and degree of fibrosis (Fig. 4a). Wall thickness measurements were performed on all sections throughout the coronal plane of the heart where the LV cavity was distinguishable. Animals treated with decorin microrods (2077 ± 399 μm) exhibited trends in having greater LV wall thickness compared to those treated with saline (1712 ± 350 μm) and free decorin (1480 ± 195 μm) and

were least different from the no MI group (2875 ± 254 μm) as seen in Fig. 4b and Table S6. Collagen fibrosis was assessed by quantifying the average intensity of Sirius red in the LV of 5 sections throughout each heart under cross-polarized imaging. Rats with no MI ($p < 0.05$) and rats treated with microrods ($p < 0.05$) and decorin microrods ($p < 0.05$) all had significantly reduced intensity of collagen staining in the LV compared to those treated with saline (Fig. 4c, Supplementary Table 6). While not statistically significant, treatment with free decorin ($p = 0.07$) also decreased average collagen intensity in the LV compared to treatment with saline.
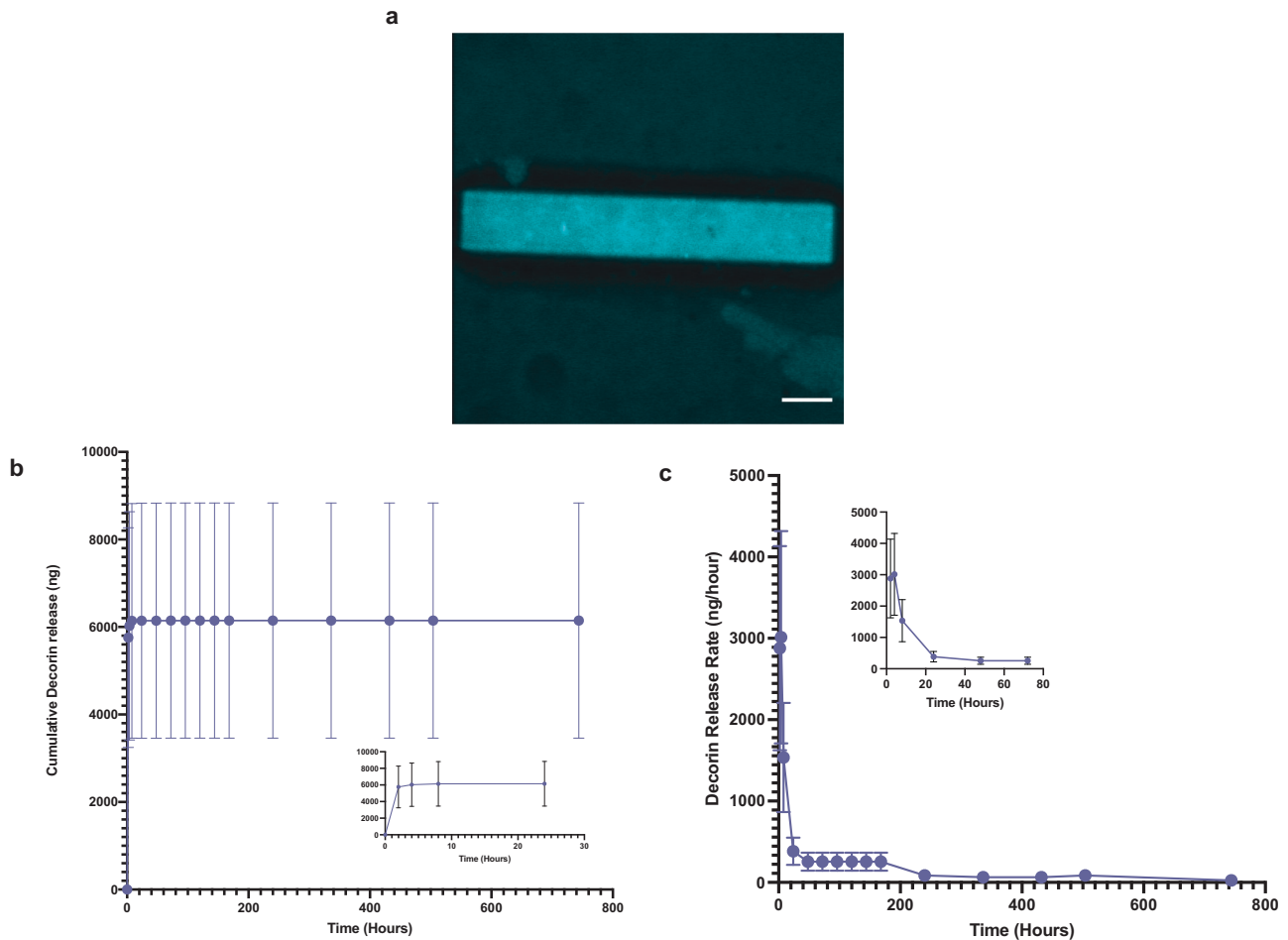
Fig. 2 Decorin loading and release profile from microrods. a Average intensity projection across ~15 μm of fluorescein-tagged decorin loaded into microrods illustrates protein loading throughout the entirety of the microrod. Scale bar = 15 μm. **b** Cumulative release (ng) and (**c**) release rate of decorin (ng/hour) from 75 mg/mL microrods over a 31-day period are shown ($n = 3$). It is apparent that decorin microrods exhibit burst release of decorin within the first 10 h (refer to inlet images) and subsequently plateau, following first-order release behavior. The data is presented as mean ± SD.

Table 1. Experimental injection groups.	
Treatment Group	Agent
No MI	None ($n = 5$)
MI + Vehicle	50 μL of 0.9% sodium chloride solution ($n = 5$)
MI + Microrods	50 μL of 50,000 microrods in 0.9% sodium chloride solution ($n = 7$)
MI + Decorin Microrods	50 μL of 50,000 decorin microrods in 0.9% sodium chloride solution ($n = 10$)
MI + Free Decorin	50 μL of 12 μg decorin in 0.9% sodium chloride solution ($n = 4$)

We also investigated the impact of decorin microrods on cardiomyocyte and endothelial cell behaviors. Given that microrods were observed to be retained in cardiac tissue for at least 8 weeks (Supplementary Fig. 5), we hypothesized that there could be additional long-term benefits bestowed by the presence of these structures. A crucial compensatory mechanism after myocardial injury is hypertrophic growth of cardiomyocytes[44]. Hypertrophy was assessed by immunofluorescence staining for sarcomeric alpha actinin, cell membrane, and nuclei in the border zone and remote zone (Fig. 5a). Three sections from throughout the heart were assessed ($n = 4$ animals per group). While no differences in cardiomyocyte area were observed between treatment groups in the border zone, reduced cardiomyocyte area in the remote zone

was identified in decorin microrod ($p < 0.05$) and free decorin-treated animals ($p < 0.01$) compared to saline-treated animals (Fig. 5b, c, Supplementary Table 7). Accordingly, we observed an increase in cardiomyocytes per area in the remote zone for decorin microrod ($p < 0.05$) and free decorin ($p < 0.05$) groups compared to the saline group (Fig. 5d, e, Supplementary Table 8). The significant increases in cardiomyocyte area, and corresponding smaller number of cardiomyocytes per area in the border zone across all treatment groups compared to the no MI group corroborates hypertrophy as a physiological response to myocardial injury. Further, morphometric analysis of cardiomyocytes indicated the observed smaller areas in decorin microrod and free decorin groups in the remote zone were due to proportional reduction in the
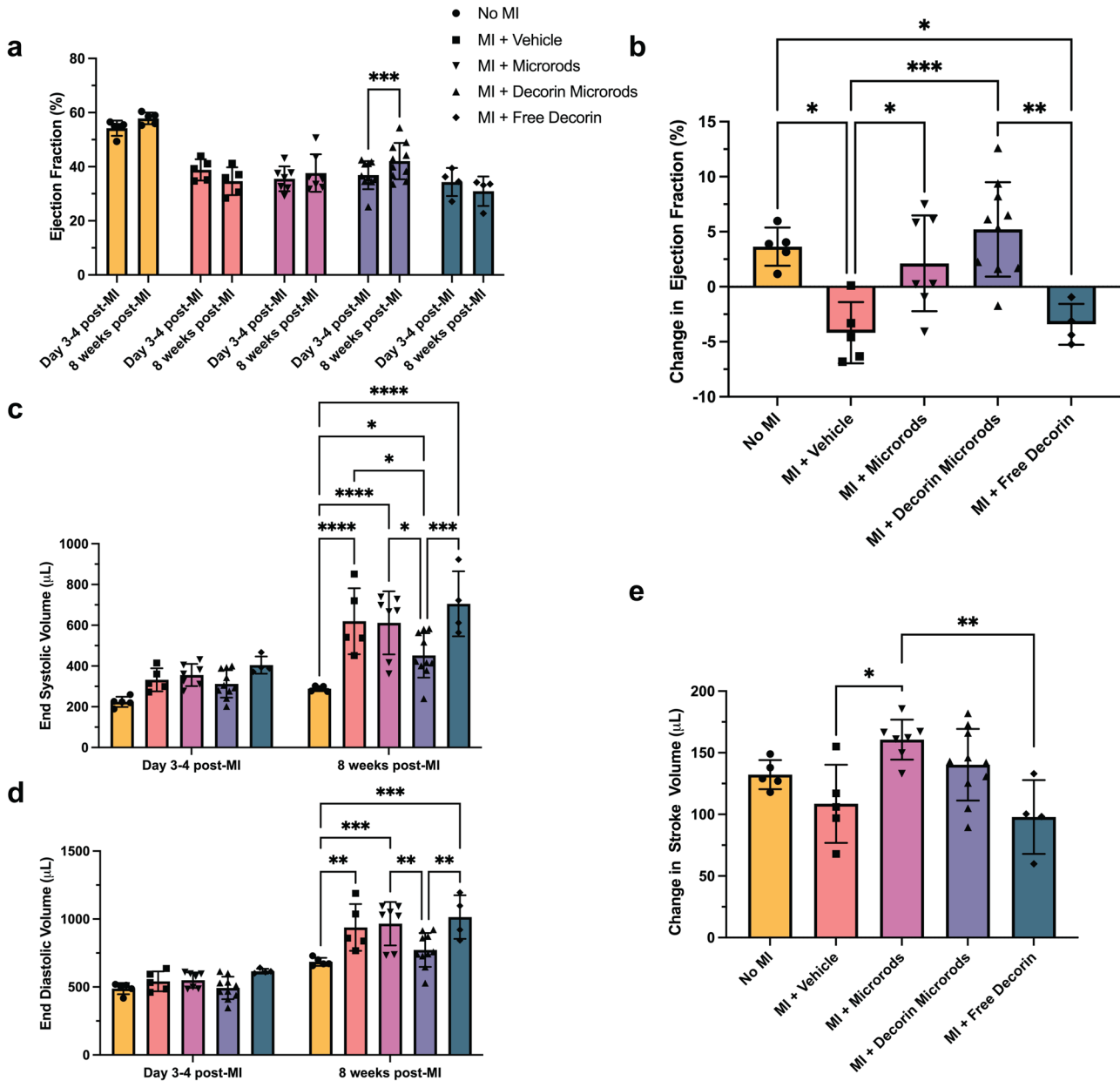
Fig. 3 Treatment with decorin microrods improves cardiac outcomes and reduces maladaptive ventricular remodeling. Echocardiography was used to compare ejection fraction (EF) at 3–4 days after infarct and at 8 weeks after infarct in rats that had no MI performed ($n = 5$) and rats with MI that were treated with saline ($n = 5$), microrods ($n = 7$), decorin microrods ($n = 10$), and free decorin ($n = 4$). **a** The average ejection fraction (EF) at 3–4 days post-MI and EF at 8 weeks post-MI for each group is plotted. While saline animals show a trend for decreased EF, decorin microrod-treated animals show significant improvement in EF over the 8-week time period. **b** Rats treated with decorin microrods and microrods had a significantly higher change in EF compared to saline-treated animals. Rats treated with decorin microrods also had a significantly higher change in EF compared to those treated with free decorin. Echocardiography was used to evaluate (**c**) end systolic volume and (**d**) end diastolic volume at 3–4 days after infarct and at 8 weeks after infarct in all experimental groups. End systolic volume and end diastolic volume were reduced in rats treated with decorin microrods compared to rats treated with saline, microrods, or free decorin. **e** Both microrod- and decorin microrod-treated animals exhibited improved change in stroke volume compared to saline and free decorin treatments. The data are presented as the mean ± SD. *$p < 0.05$, **$p < 0.01$, ***$p < 0.001$, ****$p < 0.0001$.

major/minor axes of the cells as no change in eccentricity was found across treatment groups (Supplementary Fig. 6). Studies were performed to identify if an increase in vascular density was also responsible for the observed improvements in cardiac function brought about by the decorin microrod treatment. Arteriole number was assessed by immunofluorescence staining for alpha-smooth muscle actin and nuclei in the infarct, border zone, and remote zone (Fig. 6a). Three sections from throughout the heart

were assessed ($n = 4$ animals per group). Results indicated that after 8 weeks post-MI, there were trends toward increased arteriole presence in both the microrod and decorin microrod groups compared to the free decorin in both the infarct (Fig. 6b, Supplementary Table 9; $p = 0.05$ and $p = 0.07$, respectively) and remote zones (Fig. 6d, Supplementary Table 9; $p < 0.05$ and $p < 0.001$), respectively. Further, the decorin microrod group showed a trend in improved arteriole density compared to the
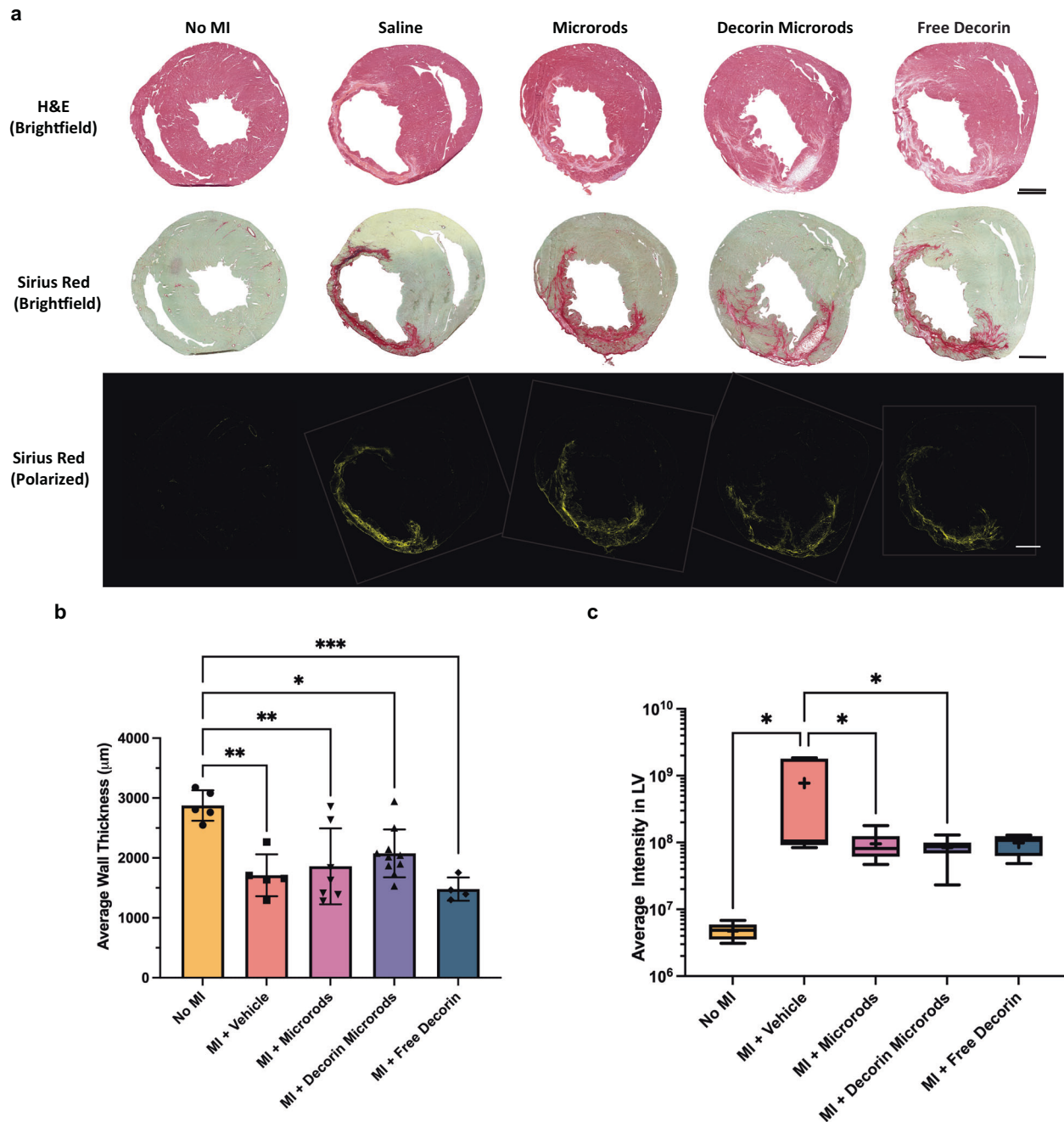
Fig. 4 Comparison of morphology and collagen content in the various treatment groups. a Histological evaluation of each treatment group was performed using H&E (top) and Sirius red (brightfield: middle, cross-polarized (pseudo-color): bottom). Scale bars = 2000 μm. **b** The average wall thickness was assessed by taking five measurements across the LV free wall in each tissue section where the LV free wall was distinguishable. Rats treated with decorin microrods showed a trend towards increased LV wall thickness compared to those treated with either saline or free decorin. The data are presented as the mean ± SD. **c** Tissue sections were stained with Sirius red and visualized under cross-polarized light. Intensity of collagen staining in the LV (including the septum) was measured using ImageJ. Treatment with microrods ($n = 7$), decorin microrods ($n = 10$), and free decorin ($n = 4$) have reduced degree of fibrosis in the LV compared to treatment with saline ($n = 5$). The mean is denoted by a "+" sign and the black whiskers represent the min and max values for each dataset. *$p < 0.05$, **$p < 0.01$, ***$p < 0.001$.

vehicle group in the remote zone (Fig. 6d, Supplementary Table 9; $p = 0.13$). Together, this data potentially indicates some therapeutic effect of the microrods on vascular potential post-MI.

DISCUSSION

An exciting area in biomaterials research focused on leveraging the mechanosensing machinery of cells has emerged in order to address the lack of effective, locally acting therapies for pathophysiological responses[7,45,46]. The ability to reliably dictate cellular responses to elicit specific phenotypes can be a powerful tool in addressing conditions that result from cardiovascular diseases, such as HF[7]. Our lab has previously shown the utility of high aspect ratio microstructures made from polypropylene and polyethylene glycol (PEG) to mitigate fibroblast transition to myofibroblasts[11,12]. However, developing therapeutic strategies

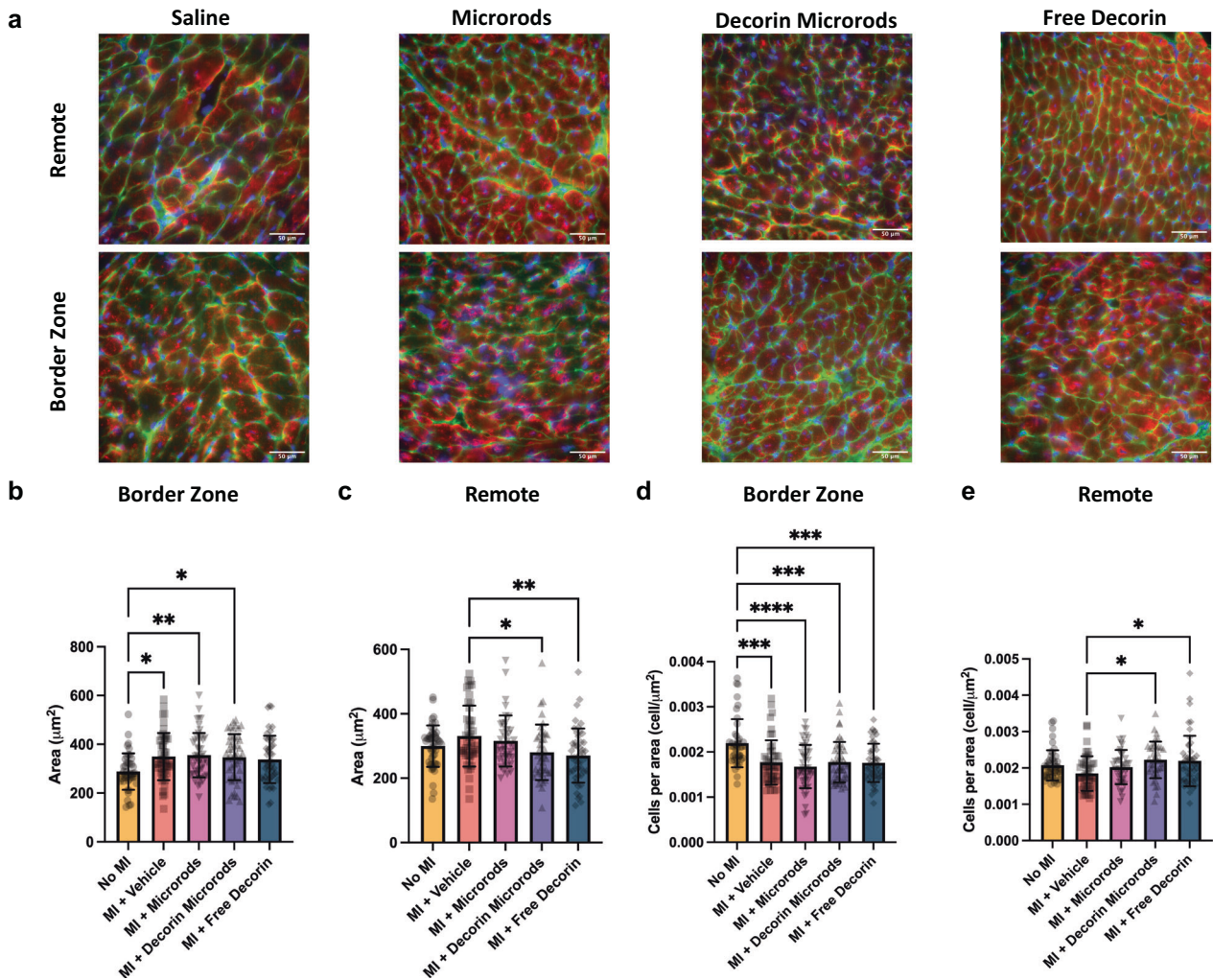**Fig. 5 Treatment with decorin microrods and free decorin decrease cardiomyocyte hypertrophy post-MI. a** Immunofluorescence staining for sarcomeric alpha actinin (red), WGA staining of cell membrane (green), and nuclei (blue) was performed to identify cardiomyocytes. Scale bars = 50 µm. Three tissue sections per heart (apex, middle, and end of the heart) were quantified for (**b, c**) cardiomyocyte area and (**d, e**) the number of cardiomyocytes per unit area in the border zone and remote zone. In cases where there was not an identifiable remote zone for a given section in a particular animal, that section was excluded from data analysis for the remote zone of that animal. Rats treated with decorin microrods and free decorin exhibited decreased cardiomyocyte area and correspondingly increased number of cardiomyocytes per unit area in the remote zone compared to rats treated with saline ($n = 4$ for all groups). The data are presented as the mean ± SD. *$p < 0.05$, **$p < 0.01$, ***$p < 0.001$, ****$p < 0.0001$.

should aim to employ materials that have biocompatibility, demonstrate favorable bioactive properties, exhibit biodegradation, and possess tunable properties for facile translation to the clinic. As such, next generation microrods were fabricated from HA, a naturally occurring polysaccharide, whose role in developing biomaterial therapies has been increasingly recognized and investigated due to its intricate involvement in several critical wound healing processes[47–51]. Advantages of employing bioactive and biodegradable materials such as HA as opposed to relatively bioinert polymers include more favorable timescales for degradation and the potential for long-acting therapeutic benefits with respect to cardiac regeneration—as HA degrades, the released oligosaccharide degradants can stimulate angiogenic processes[49,52]. HA microrods were shown to outperform other materials in attenuating fibrotic response in vitro and in improving cardiac function in in vivo models of ischemia-reperfusion MI[13]. These observed benefits are likely due to additional biochemical effects bestowed by the HA material itself.

Not only can polymeric microrods modulate cellular behaviors through mechanical regulation, but they can be formulated to release bioactive factors to achieve more robust responses. We have successfully utilized PEG microrods to locally deliver E-domain peptide and β-NGF to injured tissue in MI and tibial fracture models[14,15]. To enhance efficacy of our microrod platform for applications in post-MI therapy, we investigated the ability for microrods to locally deliver decorin, a SLRP with both anti-fibrotic and antioxidant attributes. The core protein of decorin has two binding sites for TGF-β1 and binds collagen through its leucine rich repeat region[53,54]. Several studies have implicated decorin in playing an important role in post-infarct remodeling and others have demonstrated how decorin treatment can mitigate adverse outcomes in various models of cardiovascular disease[35,37,55–57].

The improvement in cardiac metrics including change in EF, ventricular remodeling, and wall thickness that was observed in the decorin microrod-treated animals compared to microrod- and free decorin-treated animals supports recent findings regarding the ability of decorin to improve cardiovascular outcomes after injury, but also highlights the importance of delivery of the anti-fibrotic factor during wound healing. Microrods demonstrate the ability to effectively load and locally
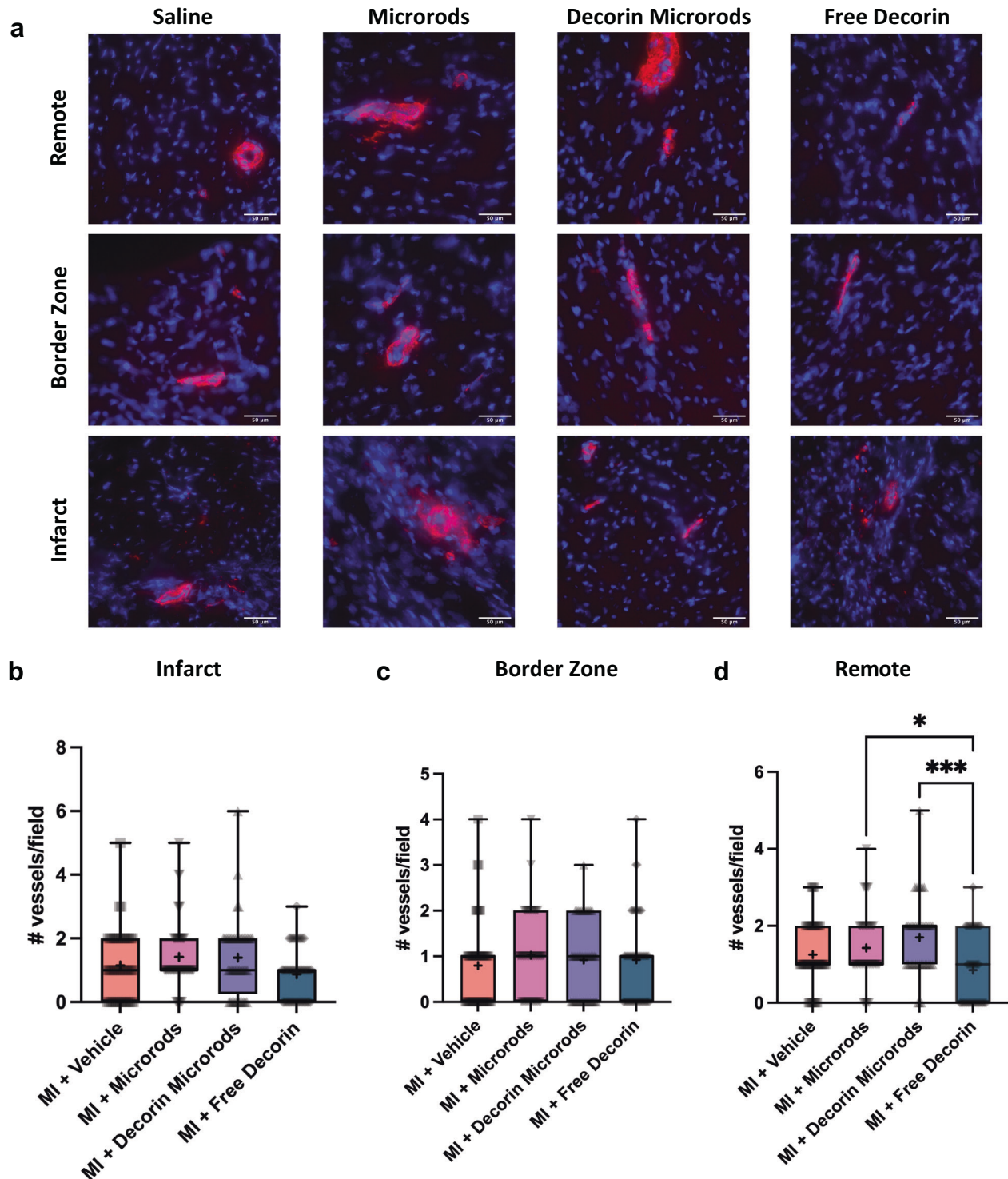
Fig. 6 Analysis of arteriole presence post-treatment. a Immunofluorescence staining for alpha smooth muscle actin (red) and nuclei (blue) was performed to identify arterioles. Scale bars = 50 μm. **b–d** Three tissue sections (apex, middle, and end of the heart) were quantified for arteriole number in the infarct, border zone, and remote zone. In cases where there was not an identifiable remote zone for a given section in a particular animal, that section was excluded from data analysis for the remote zone of that animal. Trends indicate increased number of arterioles in both microrod groups compared to free decorin (*n* = 4 for all groups). The mean is denoted by a "+" sign and the black whiskers represent the min and max values for each dataset. *$p < 0.05$, ***$p < 0.001$.

release decorin at the target site. Calculation of the theoretical mesh size of these microrods reveals a mesh size of 14.37 nm, larger than the hydrodynamic diameter of decorin reported at 9.8 ± 0.5 nm[58], thus allowing decorin to successfully be loaded into these microrods for subsequent release following injection.

We found the release of decorin to follow first-order release kinetics, with release rates depending solely on the remaining concentration of decorin in the microrod. Kinetic model fitting showed the first-order constant of this release profile to be approximately 1.36 h^{-1}.

The incorporation of decorin was hypothesized to also bestow favorable changes at the cellular level to achieve a microenvironment that is conducive to wound healing in addition to the enhanced cardiac function seen in both microrod groups compared to saline and free decorin group. Similar to findings from Faust et al. in studies utilizing decorin gene transfer, both decorin microrod- and free decorin-treated groups exhibited decreased fibrosis and cardiomyocyte hypertrophy compared to the saline-treated group[36]. Interestingly however, only rats treated with decorin microrods exhibited improved cardiac function and ventricular remodeling outcomes. Yang et al. reported that decorin decreases hypertrophic growth by regulating the calcium/calmodulin-dependent protein kinase II (CaMKII)/myocyte enhancer factor 2 (MEF-2) signaling pathway to inhibit transcription of MEF-2[59]. CAMKII has been reported to selectively phosphorylate the chromatin-modifying enzyme histone deacetylase 4 (HDAC4), which is known to maintain MEF-2 in a transcriptionally inactive state when they are associated[60,61]. Upon phosphorylation, HDAC4 dissociates from MEF-2, thereby enabling the subsequent activation of MEF-2 transcription[62]. Stress-responsive MEF-2 transcriptional activity plays a key role in regulating cardiac gene expression involved in cardiac muscle development, and has been implicated in cardiomyocytes experiencing hypertrophy[63–65]. Western blot studies demonstrated that rAAV-decorin-treated animals who had been subjected to aortic constriction exhibited decreased expression of CaMKII, p-CaMKII, and MEF-2[59]. Further experiments comparing myocyte cross-sectional size of animals treated with KN-93, a cell permeable inhibitor of CaMKII, and rAAV-decorin showcased that both KN-93 and decorin had similar effects in reducing cardiac hypertrophy[59]. This observation is in accordance with our data that demonstrated both groups that were treated with decorin had decreased cardiomyocyte hypertrophy in the remote zone. Given the differences in therapeutic outcomes regarding EF and LV volumes after 8 weeks between the two decorin-containing groups, it points to the presence of microrods as playing a role in the improved treatment efficacy. While injections of bulk HA polymers have shown to provide the myocardium with mechanical support to improve cardiac function and delay LV dilatation after injury[66–68], the injection of the microstructures acts minimally as a bulking agent to the cardiac muscle (~1uL/injection)[12]. Therefore, it is unlikely that this is the primary mechanism resulting in the observed therapeutic efficacy. Instead, it is likely a combination of these discrete cues being able to traverse tissue planes after injection to interact with widespread fibroblast populations and locally deliver decorin protein; both functions work in tandem to modulate the microenvironment to one that is less prone to fibrosis.

The increased arteriole density that was observed in both microrod groups compared to the free decorin group illustrated one of the key advantages of selecting HA as a choice material in this strategy. As HA degrades, oligosaccharides are released which are known to promote angiogenic endothelial processes including proliferation, migration, and tube formation[49,52]. However, because the injection occurred at the center of the infarct, where analysis of capillary density could be subject to high variability due to confounding variables such as tissue distortion and compression, we opted instead to investigate arteriole presence as a surrogate marker of downstream vascularization[69]. Thus, the presence and subsequent solubilization of microrods in the infarct zone may promote vessel formation. However, further investigations will need to be performed to provide more insight into this phenomenon.

The presence of HA microrods after 8 weeks is not surprising as it has been shown that methacrylated HA-based hydrogels, such as our microrods, degrade enzymatically as the hydrolytic degradation sites are sterically hindered[70]. Hyaluronidases are present at low amounts in the heart both before and after injury[71], explaining the slow degradation of these microrods. However, our

group and others have shown that when exposed to higher concentrations of hyaluronidases, these HA hydrogels will readily degrade[13,67,72]. The presence and stability of HA microrods in the myocardium may pose benefits to long-term myocardial remodeling. Previous work has shown that similar HA hydrogels improved maintenance of wall thickness, compared to more rapidly (hydrolytically) degradable HA hydrogels with similar mechanical properties otherwise. Further, these stable enzymatic HA hydrogels elicited less inflammatory cues from the surrounding cells compared to their degradable counterparts[70]. The immunomodulatory role that these HA microrods have within the infarct microenvironment still requires further examination, but similar HA hydrogels have been reported to elicit minimal inflammation and favorable cytocompatibility[73]. The long-term presence of HA microrods may play a beneficial role within the myocardium remodeling, as the extended stability of similar HA gels has led to prolonged reduction in LV volume compared to degradable systems[70]. We have also previously seen that HA microrods do not affect the contractility of cardiomyocytes[13]. The long-term effects of HA microrods and similar HA hydrogel systems in the myocardium have not been well explored and require further longitudinal studies to understand the myriad of cell-material and cell-cell interactions that HA systems affect.

While our results are promising, we recognize that there may exist some limitations to the work described here. The animal studies shown utilized male Sprague-Dawley rats to ensure that consistent models of HF were achieved. Of note, it has been documented that there may exist differences in post-MI left ventricular remodeling based that is influenced by sex. Prior studies have demonstrated favorable remodeling processes in females compared to males after myocardial injury that may be due to the ability to retain advantageous myocardial properties, such as reduced myocyte apoptosis and hypertrophy[74–78]. These sex-related differences in remodeling responses post-MI may also explain why in the prior investigation using all female rats, the HA microrod group appeared to have a more pronounced improvement in cardiac performance compared to what was observed in the microrod groups in this study[13]. To better account for differences in therapeutic response based on sex, future studies involving both male and female rats are necessary. Additionally, while power analysis shows that we were able to achieve significant power in the current study, future work will benefit from larger sample sizes. By identifying the relevant pathways and physiological responses that are affected by these microstructures, it will be possible to optimize this therapeutic strategy to achieve more holistic myocardial repair after injury.

In this work, we investigated the capacity for polymeric microrods made of hyaluronic acid to locally deliver the anti-fibrotic agent decorin to the infarct and modulate the post-infarct environment to dampen pathophysiological responses that occur post-MI. Our results demonstrate the ability for a dual, biochemical and biophysical therapeutic strategy to improve cardiac and ventricular remodeling outcomes while simultaneously attenuating collagen fibrosis and cardiomyocyte hypertrophy in preclinical models of I/R MI. Therefore, the use of decorin microrods represents a promising and novel translational strategy for cardiac treatment after MI. Applications of this biophysical platform in additional clinically relevant models including bone healing, cirrhosis, and implantable devices represents exciting prospects to further advance our ability to facilitate wound healing and tissue repair.

METHODS

Synthesis of hyaluronic acid methacrylate

Hyaluronic acid methacrylate (HAMA) was synthesized based on a protocol adapted from Bencherif et al.[79] These methods have

been previously reported by our lab[13]. Briefly, one gram of sodium hyaluronate (100 kDa, Lifecore Biomedical, Chaska, MN) was dissolved at 3.76 mg/mL in a 1:1 solution of deionized (DI) water: dimethylformamide (266 mL, Sigma-Aldrich, St. Louis, MO). After solubilizing, a 73-fold molar excess of glycidyl methacrylate (24.86 mL, 0.1822 mol, Sigma-Aldrich) and 26.5-fold molar excess of triethylamine (9.235 mL, 0.066 mol, Sigma-Aldrich) with respect to the primary hydroxyl/hydroxymethyl functional group on hyaluronic acid was added to the mixture. The reaction was left to stir for 24 h at ambient temperature while protected from light. HA and HAMA products were recovered via precipitation in an excess of isopropanol. Briefly, 35 mL of isopropanol was added to 15 mL of reaction solution and then the precipitate was isolated by centrifugation at 1275 × g for 5 min. This process was repeated until all of the reaction solution had been precipitated. The recovered precipitate was subsequently dissolved in 90 mL of DI water. The resulting solution was then dialyzed (Spectrum™ Spectra/Por™ 3 RC dialysis membrane tubing, 3500 Dalton MWCO, Thermo Fischer Scientific 08-670-5B, Waltham, MA) against DI water (10 times volume of the solution) for 48 h with three changes of water. The product was then lyophilized for 3–4 days at −40 °C and 65 mTorr and the resulting white powder was then stored at −20 °C until further use. ^{1}H NMR spectroscopy (Bruker Avance III HD 400 NMR) was used to determine the degree of methacrylation. Methacrylate peaks are observed at ~6.5, ~5.6, and ~1.85 ppm. Degree of methacrylation was calculated based on the ratio of the relative peak integration of the methacrylate peak at 1.85 ppm and HA's acetamide peak which occurs at 1.9 ppm and was determined to be ~50.1 ± 6.9% substitution (data not shown).

Hyaluronic acid microrod fabrication

HAMA was dissolved at 75 mg/mL in DI water containing 0.5% w/v of the photoinitiator 2-hydroxy-4′-(2-hydroxyethoxy)-2-methylpro-piophenone (Sigma-Aldrich 410896). The solution was stirred for 2 h at ambient temperature to facilitate solubilization and protected from light. After, the solution was centrifuged at 15000 × g for 5 min to remove any impurities. Subsequently, a 15 μm layer of precursor solution was deposited onto an oxygen plasma- or piranha-treated 3 in. silicon wafer. The wafer was then patterned using a Karl Suss MJB3 or Quintel Q4000 mask aligner by exposing the wafer through a photomask (15 μm × 100 μm features) to a 365 nm UV light source. Crosslinked microrods were then gently removed from the wafer using a cell scraper and collected into DI water, where any uncrosslinked HAMA would fully dissolve. Microrods were then passed through a 150 μm mesh filter to remove any aggregates and then concentrated by centrifugation. The microrods were subsequently sterilized with 70% ethanol for 30 min and then resuspended in saline prior to use. Microrod concentration was determined using a hemocytometer by counting the number of microrods that appeared in the nine gridded boxes after pipetting 10 μL of microrod solution into the hemocytometer. The number of counted microrods was then divided by 9, and then multiplied by 10^4 and the dilution factor to get the microrod concentration in the stock solution. The microfabrication process is illustrated in Fig. 1.

Decorin loading of microrods

To passively load microrods with decorin (Abcam ab167743, Cambridge, UK), 750,000 microrods were concentrated in 1 mL of DI water and then 333 μL of decorin (600 μg/mL) was added. The microrods were passively loaded via incubation with inversion over 4 days at 4 °C. After incubation, the microrods were centrifuged at 15,000 × g for 10 min and the supernatant was removed. The microrods were then recentrifuged at 15,000 × g for 10 min once more to concentrate them and remove any residual solution. The microrods were then resuspended in saline to the desired concentration. Decorin loading was assessed via NanoOrange Protein Quantitation Kit (Thermo Fisher Scientific N6666). Values were validated with an ELISA for human decorin (Abcam ab99998) (data not shown). Decorin loading was determined by calculating the amount of free decorin in the supernatant post-centrifugation, and then subtracting that value from the initial amount of decorin added (200 μg), and then dividing that value by 750,000 to get the amount of decorin (μg) per microrod.

To visualize the loading of decorin within the microrods, decorin was tagged with fluorescein-5-maleimide (Thermo Fisher Scientific 62245) through thiol-maleimide chemistry following the manufacturer's protocol. Briefly, decorin was solubilized in PBS with 10 mM ethylenediaminetetraacetic acid (EDTA) (Research Products International E5704, Mt. Prospect, IL) and reduced with 100x molar excess tris (2-carboxyethyl) phosphine (TCEP) (Sigma-Aldrich 646547) to expose sulfhydryl groups of the cysteines within the protein. Fluorescein-5-maleimide was added at 15-fold molar excess to the solution and the reaction proceeded at ambient temperature for 2 h. Conjugated protein was then concentrated using a Pierce 10k molecular weight cutoff spin column (Thermo Fisher Scientific 88513) to remove non-conjugated fluorescein. Fluorescein-tagged decorin was then loaded into hyaluronic acid microrods following the method described previously and imaged on a Nikon spinning disk confocal microscope.

Calculation of theoretical mesh size of HA microrods

The mesh size (ξ) of HA microrods was calculated using the universal Canal-Peppas Equation described by Richbourg and Peppas (Eq. (1))[80].

$$\xi = \varphi^{-\frac{1}{3}}\left(\left(1 - \frac{2}{f}\right)\bar{l}^2 C_\infty \frac{\lambda \overline{M_c}}{M_r}\right)^{\frac{1}{2}} \tag{1}$$

Where φ is the general polymer volume fraction, f is the junction functionality in the polymer network, $\bar{l}$ is the weighted average of bond lengths per repeating unit, C_∞ is the polymer-specific characteristic ratio for a long chain, λ is the polymer backbone bond factor, $\overline{M_c}$ is the average molecular weight between crosslinks, and M_r is the molecular weight of the polymer repeat unit. Values determined from our fabrication formulation alongside values identified in literature[81–83] were utilized to perform these calculations.

Decorin release study from microrods

After loading, decorin microrods were divided into Protein Lo-Bind tubes (Eppendorf 022431102, Hamburg, Germany) consisting of 50,000 microrods/microcentrifuge tube, and then suspended in 1 mL of phosphate buffered saline (PBS) containing 0.05% Tween-20 (pH 7.4). Samples were placed onto a tube revolver (14 RPM) within an incubator (37 °C). Decorin microrods were spun down at 8000 RPM for 3 min and the entire supernatant was collected and replenished with 1 mL at 4, 8, 16, 24, 72, 96, 120, 144, 168, 240, 336, 432, 504, and 744 h. Collected supernatants were immediately flash frozen and stored at −80 °C until further use. An ELISA for human decorin (Abcam) was performed per the manufacturer's instructions and hourly release amounts were calculated using an established standard curve using human decorin (Abcam).

Collagen turbidity assay

First, a 1 mg/mL stock solution of collagen type I (Thermo Fischer Scientific CB354249) was prepared by diluting high concentration collagen type I with PBS and then was subsequently kept on ice along with a 96-well plate. Varying decorin concentrations ranging from 5–80 μg/mL were then prepared by diluting 600 μg/mL stock decorin solution with PBS. Then, a 1:1 ratio of 1 mg/mL collagen type I and the decorin stocks were added to each well in triplicate

resulting in final decorin doses of 2.5, 5, 10, 20, and 40 μg/mL. Absorbance measurements at 405 nm were then taken every 5 min over the span of 2 h at ambient temperature using a plate reader. The assay also included blank controls of water and PBS as well as a control for the highest concentration of decorin (40 μg/mL).

Cell culture & qCPR

NIH 3T3 mouse fibroblasts (ATCC, Manassas, Virginia) were cultured in Dulbecco's modified Eagle's medium with 10% fetal calf serum and 1% penicillin/streptomycin. Cells were seeded into 24-well plates and then media was added that either contained 10 ng/mL TGF-β1 (PeproTech 100-21) or 10 ng/mL TGF-β1 plus 10 μg/mL decorin. Genetic material was harvested and purified using the RNeasy Mini Kit (Qiagen, Hilden, Germany). RNA was converted into cDNA using the iScript cDNA synthesis kit (Bio-Rad Laboratories, Hercules, CA) and a Viia7 qPCR machine (Life Technologies, Carlsbad, CA) was used to measure relative expression levels of gene targets compared to the housekeeping gene 60 S ribosomal protein L19. Expression levels of all genes were evaluated using the Fast SYBR Green Mastermix (Life Technologies, Grand Island, NY) and custom DNA primers (Integrated DNA Technologies, Coralville, IA) in triplicate for three biological replicates (Table S1).

Infarct model and microrod injections

The animal protocol for MI induction was approved by the Committee for Animal Research of the University of California, San Francisco and was performed in accordance with the recommendations of the American Association for Accreditation of Laboratory Animal Care. The ischemia reperfusion (I/R) MI model used in this study has been extensively tested and successfully used in our labs[12,13,84,85]. To produce the MI model, male Sprague-Dawley rats (200–225 g) underwent occlusion of the left anterior descending coronary artery for 30 min followed by reperfusion while under general anesthesia which was achieved by inhalation of 2% L/min isoflurane[84]. This study utilized all male Sprague-Dawley rats to achieve consistent models of HF as prior studies have identified sex-related differences in remodeling responses post-MI[74–78]. The chest was then sutured closed, and the animal was allowed to recover. After 3–4 days, the rats were randomized to saline-injected, microrod-injected, decorin microrod-injected, or free decorin-injected treatment groups (Table 1), and were given one intramuscular injection into the myocardial wall via ultrasound guided transthoracic injection using a 29-gauge syringe under blinded conditions[12,13,84,86]. Successful injection to the center of the infarct region was confirmed by a local increase in ultrasound signal and brief thickening of the left ventricle (LV) wall near the tip of the syringe.

Echocardiography

Transthoracic echocardiography was performed with a 15-MHz linear array transducer system (Vevo 3100LT, FUJIFILM VisualSonics, Ontario, Canada) on all animals while under general anesthesia (2% L/min isoflurane). Echocardiography was performed prior to injection on either day 3 or 4 and 8 weeks post-MI using standard methods that have been performed reproducibly in our lab[12,13,84,86]. To determine LV end systolic volume (LVESV), LV end diastolic volume (LVEDV), and ejection fraction (EF) at 3–4 days and 8 weeks post-MI, the LV endocardium was outlined in both the end-systolic and end-diastolic phase and the single plane area length algorithmic method was applied. Additionally, two-dimensional images were obtained in both parasternal long- and short-axis views at the papillary muscle level. Stroke volume (SV) was calculated by $SV = LVEDV-LVESV$, while change in EF was calculated by $\Delta EF = EF_{8 \text{ weeks post-MI}} - EF_{3-4 \text{ days post-MI}}$. All images were taken and subsequently analyzed in a blinded manner. In situations where the ventricular endocardium was not clearly identifiable in the 3–4 days or 8-week post-MI image, the animal was excluded from echocardiographic analyses. Cases where EF was above 45% at 3–4 days post-MI were excluded because they indicated an insufficient infarct model.

Histology

Sacrifice was performed at 8 weeks post-MI after performing endpoint echocardiography. The animal was maintained at 5% L/min isoflurane for 5 min, followed by bilateral thoracotomy and injection of potassium chloride into the right atrium to arrest the heart in diastole. The heart was then extracted and frozen in OCT (Sakura Finetech USA, Inc., Torrance, CA) using 2-methylbutane (Sigma-Aldrich) on dry ice and sectioned for histology, immuno-fluorescence imaging, and subsequent image analysis. Tissue blocks of cardiac tissue were cryo-sectioned at a thickness of 10 μm starting at the apex of the LV, collecting ten serial sections every 350 μm until a total of 100 sections were collected. Sections were stained with H&E and Sirius red using standard protocols. Briefly for Sirius red staining, frozen sections were brought to room temperature, soaked in xylene for a total of 15 min., rehydrated using an ethanol series (100%, 95%, and 80%) for 1 min. each, and then soaked in water. Sections were then incubated in 0.01% Fast Green FCF solution (Sigma-Aldrich F7252) in saturated picric aqueous solution (Sigma-Aldrich P6744) for 1 h. followed by a 1 h. incubation in 0.04% Fast Green FCF/0.1% Sirius red (Sigma-Aldrich 365548) in saturated picric acid solution. Next, sections were dipped in acidified water, 100% alcohol, and then xylene prior to mounting. For H&E staining, slides were soaked in tap water for 5 min to remove OCT from the sections. They were then stained in Harris's Hematoxylin (VWR 95057-858, Radnor, PA) for 5 min., followed by dipping in water for 1 min, and then dipping in Differentiating Solution (Sigma-Aldrich A3179) for 1 s for a total of three times. Next, slides were immersed in Bluing Solution (0.1% sodium bicarbonate, pH ~8.0) for 30 s, followed by dipping in water for 1 min. Slides were then soaked in 70% ethanol for 1 min. and then in Eosin Y Solution (VWR 95057-848) for 45 sec. Sections were dehydrated using an ethanol series (85%, 95%, 100%) for 1 min. each before soaking in xylene and mounting. For immunofluorescence stains, tissue sections were fixed in acetone and blocked with 10% serum, followed by incubation with primary and secondary antibodies using standard protocols. In brief, samples were first rinsed in DI water for 10 min. and allowed to air dry for 1 h. Then, they were fixed in ice cold acetone for 5 min., blocked with 10% serum for 20 min., and incubated overnight with anti-sarcomeric alpha actin (1:500, Abcam ab137346) and anti-alpha smooth muscle actin (1:500, Abcam ab5694) at 4 °C in a solution of 0.05% Tween-20/10% serum/1% BSA in PBS After washing, secondary antibody and WGA (1:100, Thermo Fisher Scientific W11261) were added for 45 min at room temperature. Hoechst (1:500, Thermo Fisher Scientific 33342) was added for 5 min at room temperature to visualize nuclei.

Imaging and quantification

For whole heart histology, images were taken using a Nikon 6D optical microscope (NIKON Instruments, Inc., Melville, NY) using 4–40x objectives (H&E and Sirius red). Subsequent quantifications were performed using custom scripts and ImageJ.

For collagen analysis, five alternating sections of each heart were selected from throughout the coronal plane of the heart and stained with Sirius red to assess the quantity and density of collagen in the infarcted hearts. These sections were imaged under brightfield as well as under cross-polarized light to visualize the collagen fibers using a 4x objective. Representative images for brightfield and polarized shading corrections were taken prior to the start of each imaging session. Infarct area and intensity were quantified in the LV,

which included the septum. Intensity measurements in the regions of interest were determined using ImageJ.

For wall thickness analysis, five measurements across the LV free wall were recorded for each tissue section where the LV free wall was distinguishable using ImageJ. The average length across all analyzed sections in each heart sample was reported.

For cardiomyocyte cross-sectional area analysis, three sections (apex, middle, and end of the heart) per heart ($n = 4$ per group) were selected and stained with anti-sarcomeric alpha actinin, WGA, and Hoechst. Four high-magnification (40x objective) images of the border zone and remote zone in each section, for each animal were averaged to obtain the cross-sectional area, cells per area, eccentricity, major axis length, and minor axis length. In cases where there was not an identifiable remote zone for a given section in a particular animal, that section was excluded from data analysis for the remote zone of that animal. Specifically, WGA-stained sections aided in the determination of number of cells per area and were quantified in Python (3.9.7) using OpenCV (4.5.5.64) and scikit-image (0.18.3) packages to conduct watershed thresholding of cell bodies and subsequent area measurements[87,88]. Images were inverted and then binarized using an adaptive mean threshold before applying the watershed segmentation algorithm. The area of segmented cells, cell count per area, eccentricity, major axis length, and minor axis length were then computed. Segmented images were then manually checked to ensure good quality segmentation, with those showing a high error rate excluded (e.g., high fractionation of cells into multiple segments, doublet or multiplet cells recognized as one cell body, membrane stains segmented as cells). For each image, the average cell area, number of cells per μm^2, eccentricity, major axis, and minor axis are reported.

For vascular density analysis, three sections (apex, middle, and end of the heart) per heart ($n = 4$ per group) were selected and stained with anti-alpha smooth muscle actin and Hoechst. Four high-magnification (40x objective) images of the remote, infarct, and border zone regions in each section, for each animal were averaged to obtain the number of arterioles per field. Only vessels that stained positively for alpha smooth muscle actin and possessed a visible lumen were included in the analysis. In cases where there was not an identifiable remote zone for a given section in a particular animal, that section was excluded from data analysis for the remote zone of that animal.

Statistical analysis

All data are presented as the mean ± standard deviation unless otherwise indicated. All statistical analysis was performed using GraphPad Prism v9.5.1. In vitro gene expression analysis was performed using a two-tailed student's t-test to identify statistical differences between two groups. One-way analysis of variance (ANOVA), followed by the Tukey's multiple comparisons test was used to identify differences between three or more groups, unless otherwise stated. Statistical comparisons made within groups to assess differences in EF between days 3–4 and 8 weeks post-MI were made using two-way repeated measures ANOVA followed by the Šidák's multiple comparisons test. Statistical comparisons made between groups to assess differences in collagen turbidity over 120 mins. and LVESV/LVEDV at 8 weeks post-MI were made using a two-way repeated measures ANOVA followed by the Tukey's multiple comparisons test. Power analysis was performed using G*Power.

Reporting summary

Further information on research design is available in the Nature Research Reporting Summary linked to this article.

REFERENCES

1. Virani, S. S. et al. Heart disease and stroke statistics—2021 update. *Circulation* **143**, E254–E743 (2021).
2. Roger, V. L. Epidemiology of heart failure. *Circ. Res.* **113**, 646 (2013).
3. Wu, T. et al. Minimal evidence of transdifferentiation from recipient bone marrow to parenchymal cells in regenerating and long-surviving human allografts. *Am. J. Transpl.* **3**, 1173–1181 (2003).
4. Tang, X. L. et al. Long-term outcome of administration of c-kitPOS cardiac progenitor cells after acute myocardial infarction: transplanted cells do not become cardiomyocytes, structural and functional improvement and proliferation of endogenous cells persist for at least one year. *Circ. Res.* **118**, 1091 (2016).
5. Rosenbloom, J., Mendoza, F. A. & Jimenez, S. A. Strategies for anti-fibrotic therapies. *Biochim. Biophys. Acta.* **1832**, 1088–1103 (2013).
6. Denton, C. P. et al. Recombinant human anti-transforming growth factor beta1 antibody therapy in systemic sclerosis: a multicenter, randomized, placebo-controlled phase I/II trial of CAT-192. *Arthritis Rheum.* **56**, 323–333 (2007).
7. Mohindra, P. & Desai, T. A. Micro- and nanoscale biophysical cues for cardiovascular disease therapy. *Nanomed. Nanotechnol. Biol. Med.* **34**, 102365 (2021).
8. Souders, C. A., Bowers, S. L. K. & Baudino, T. A. Cardiac fibroblast: the renaissance cell. *Circ. Res.* **105**, 1164 (2009).
9. Travers, J. G., Kamal, F. A., Robbins, J., Yutzey, K. E. & Blaxall, B. C. Cardiac Fibrosis. *Circ. Res.* **118**, 1021–1040 (2016).
10. Ayala, P., Lopez, J. I. & Desai, T. A. Microtopographical cues in 3D attenuate fibrotic phenotype and extracellular matrix deposition: implications for tissue regeneration. *Tissue Eng. Part A* **16**, 2519 (2010).
11. Allen, J. et al. Tunable microfibers suppress fibrotic encapsulation via inhibition of TGFβ signaling. *Tissue Eng. Part A* **22**, 142 (2016).
12. Pinney, J. R. et al. Discrete microstructural cues for the attenuation of fibrosis following myocardial infarction. *Biomaterials* **35**, 8820 (2014).
13. Le, L. V. et al. Injectable hyaluronic acid-based microrods provide local micromechanical and biochemical cues to attenuate cardiac fibrosis after myocardial infarction. *Biomaterials* **169**, 11–21 (2018).
14. Peña, J. R., Pinney, J. R., Ayala, P., Desai, T. A. & Goldspink, P. H. Localized delivery of mechano-growth factor E-domain peptide via polymeric microstructures improves cardiac function following myocardial infarction. *Biomaterials* **46**, 26–34 (2015).
15. Rivera, K. O. et al. Localized delivery of β-NGF via injectable microrods accelerates endochondral fracture repair. *Front. Bioeng. Biotechnol.* 2023.05.22. https://doi.org/10.3389/fbioe.2023.1190371 (2023).
16. Neri, M., Riezzo, I., Pascale, N., Pomara, C. & Turillazzi, E. Ischemia/reperfusion injury following acute myocardial infarction: a critical issue for clinicians and forensic pathologists. *Mediators Inflamm.* **2017**, 7018393 (2017).
17. Verma, S. et al. Fundamentals of reperfusion injury for the clinical cardiologist. *Circulation* **105**, 2332–2336 (2002).
18. Takawale, A. et al. Myocardial recovery from ischemia-reperfusion is compromised in the absence of tissue inhibitor of metalloproteinase 4. *Circ. Hear. Fail.* **7**, 652–662 (2014).
19. van der Pol, A., van Gilst, W. H., Voors, A. A. & van der Meer, P. Treating oxidative stress in heart failure: past, present and future. *Eur. J. Heart Fail* **21**, 425–435 (2019).
20. Jugdutt, B. I. & Jugdutt, B. A. Role of oxidative stress in myocardial ischemia and infarction. *Oxidative Stress Hear. Dis.* 325–362 https://doi.org/10.1007/978-981-13-8273-4_14/TABLES/3 (2019).
21. Wang, R. M. et al. Myocardial matrix hydrogel acts as a reactive oxygen species scavenger and supports a proliferative microenvironment for cardiomyocytes. *Acta Biomater.* **152**, 47–59 (2022).
22. Wang, S. et al. Preservation of cardiac functions post myocardial infarction in vivo by a phenylboric acid-grafted hyaluronic hydrogel with anti-oxidation and

23. Talman, V. & Ruskoaho, H. Cardiac fibrosis in myocardial infarction—from repair and remodeling to regeneration. *Cell Tissue Res.* **365**, 563 (2016).

24. Hinderer, S. & Schenke-Layland, K. Cardiac fibrosis—A short review of causes and therapeutic strategies. *Adv. Drug Deliv. Rev.* **146**, 77–82 (2019).

25. Yue, T. et al. Multifunctional biomaterial platforms for blocking the fibrosis process and promoting cellular restoring effects in myocardial fibrosis therapy. *Front. Bioeng. Biotechnol.* **10**, 1544 (2022).

26. Diaz, M. D. et al. Injectable myocardial matrix hydrogel mitigates negative left ventricular remodeling in a chronic myocardial infarction model.*JACC Basic Transl.Sci.* **6**, 350–361 (2021).

27. Kalamajski, S. & Oldberg, A. The role of small leucine-rich proteoglycans in collagen fibrillogenesis. *Matrix Biol.* **29**, 248–253 (2010).

28. Reese, S. P., Underwood, C. J. & Weiss, J. A. Effects of decorin proteoglycan on fibrillogenesis, ultrastructure, and mechanics of type I collagen gels. *Matrix Biol.* **32**, 414–423 (2013).

29. Iwasaki, S. et al. The modulation of collagen fibril assembly and its structure by decorin: an electron microscopic study. *Arch. Histol. Cytol.* **71**, 37–44 (2008).

30. Raspanti, M., Viola, M., Sonaggere, M., Tira, M. E. & Tenni, R. Collagen fibril structure is affected by collagen concentration and decorin. *Biomacromolecules* **8**, 2087–2091 (2007).

31. Rada, J. A., Cornuet, P. K. & Hassell, J. R. Regulation of corneal collagen fibrillogenesis in vitro by corneal proteoglycan (lumican and decorin) core proteins. *Exp. Eye Res.* **56**, 635–648 (1993).

32. Yamaguchi, Y., Mann, D. M. & Ruoslahti, E. Negative regulation of transforming growth factor-beta by the proteoglycan decorin. *Nature* **346**, 281–284 (1990).

33. Hildebrand, A. et al. Interaction of the small interstitial proteoglycans biglycan, decorin and fibromodulin with transforming growth factor beta. *Biochem. J.* **302**, 527–534 (1994).

34. Hill, L. J. et al. Sustained release of decorin to the surface of the eye enables scarless corneal regeneration. *NPJ Regen. Med.* **3**, 23 (2018).

35. Alan, C., Kocoglu, H., Altintas, R., Alici, B. & Ersay, A. R. Protective effect of decorin on acute ischemia-reperfusion injury in the rat kidney. *Arch. Med. Sci.* **7**, 211–216 (2011).

36. Faust, S. M., Lu, G., Wood, S. C. & Bishop, D. K. Transforming growth factor β neutralization within cardiac allografts by decorin gene transfer attenuates chronic rejection. *J. Immunol.* **183**, 7307 (2009).

37. Li, L. et al. Postinfarction gene therapy with adenoviral vector expressing decorin mitigates cardiac remodeling and dysfunction. *Am. J. Physiol. Heart Circ. Physiol.* **297**, H1504–H1513 (2009).

38. Zhang, Z. et al. Recombinant human decorin inhibits TGF-β1-induced contraction of collagen lattice by hypertrophic scar fibroblasts. *Burns* **35**, 527–537 (2009).

39. Mohan, R. R., Gupta, R., Mehan, M. K., Cowden, J. W. & Sinha, S. Decorin transfection suppresses profibrogenic genes and myofibroblast formation in human corneal fibroblasts. *Exp. Eye Res.* **91**, 238–245 (2010).

40. Kwan, P., Ding, J. & Tredget, E. E. MicroRNA 181b regulates decorin production by dermal fibroblasts and may be a potential therapy for hypertrophic scar. *PLoS One* **10**, e0123054–e0123054 (2015).

41. Özay, R. et al. Does decorin protect neuronal tissue via its antioxidant and anti-inflammatory activity from traumatic brain injury? an experimental study. *World Neurosurg.* **97**, 407–415 (2017).

42. Du, S., Shao, J., Xie, D. & Zhang, F. Decorin inhibits glucose-induced lens epithelial cell apoptosis via suppressing p22phox-p38 MAPK signaling pathway. *PLoS One* **15**, e0224251 (2020).

43. Santra, M. et al. Protection of adult mouse progenitor cells and human glioma cells by de novo decorin expression in an oxygen- and glucose-deprived cell culture model system. *J. Cereb. Blood Flow. Metab.* **26**, 1311–1322 (2006).

44. Gerdes, A. M. & Capasso, J. M. Structural remodeling and mechanical dysfunction of cardiac myocytes in heart failure. *J. Mol. Cell. Cardiol.* https://doi.org/10.1016/0022-2828(95)90000-4 (1995).

45. Le, L. V., Mkrtschjan, M. A., Russell, B. & Desai, T. A. Hang on tight: reprogramming the cell with microstructural cues. *Biomed. Microdevices* **21**, 43 (2019).

46. Kharbikar, B. N., Mohindra, P. & Desai, T. A. Biomaterials to enhance stem cell transplantation. *Cell Stem Cell* **29**, 692–721 (2022).

47. Slevin, M. et al. Hyaluronan-mediated angiogenesis in vascular disease: uncovering RHAMM and CD44 receptor signaling pathways. *Matrix Biol.* **26**, 58–68 (2007).

48. Yang, C. et al. The high and low molecular weight forms of hyaluronan have distinct effects on CD44 clustering. *J. Biol. Chem.* **287**, 43094 (2012).

49. Gao, F., Yang, C. X., Mo, W., Liu, Y. W. & He, Y. Q. Hyaluronan oligosaccharides are potential stimulators to angiogenesis via RHAMM mediated signal pathway in wound healing. *Clin. Investig. Med.* **31**, E106–E116 (2008).

50. Abdalla, S., Makhoul, G., Duong, M., Chiu, R. C. J. & Cecere, R. Hyaluronic acid-based hydrogel induces neovascularization and improves cardiac function in a rat model of myocardial infarction. *Interact. Cardiovasc. Thorac. Surg.* **17**, 767 (2013).

51. Hemshekhar, M. et al. Emerging roles of hyaluronic acid bioscaffolds in tissue engineering and regenerative medicine. *Int. J. Biol. Macromol.* **86**, 917–928 (2016).

52. Wang, Y., Han, G., Guo, B. & Huang, J. Hyaluronan oligosaccharides promote diabetic wound healing by increasing angiogenesis. *Pharmacol. Rep.* **68**, 1126–1132 (2016).

53. Takeuchis, Y., Kodama, Y. & Matsumoto, T. Bone matrix decorin binds transforming growth factor+ and enhances its bioactivity*. *J. Biol. Chem.* **269**, 3263632638 (1994).

54. Gubbiotti, M. A., Vallet, S. D., Ricard-Blum, S. & Iozzo, R. V. Decorin interacting network: a comprehensive analysis of decorin-binding partners and their versatile functions. *Matrix Biol.* **55**, 7 (2016).

55. Weis, S. M. et al. A role for decorin in the remodeling of myocardial infarction. *Matrix Biol.* **24**, 313–324 (2005).

56. Hao, J. et al. Elevation of Expression of Smads 2, 3, and 4, Decorin and TGF-βin the Chronic Phase of Myocardial Infarct Scar Healing. *J. Mol. Cell. Cardiol.* **31**, 667–678 (1999).

57. Yan, W. et al. Decorin gene delivery inhibits cardiac fibrosis in spontaneously hypertensive rats by modulation of transforming growth factor-β/smad and p38 mitogen-activated protein kinase signaling pathways. *Hum. Gene. Ther.* **20**, 1190–1200 (2009).

58. Scott, P. G., Grossmann, J. G., Dodd, C. M., Sheehan, J. K. & Bishop, P. N. Light and X-ray scattering show decorin to be a dimer in solution. *J. Biol. Chem.* **278**, 18353–18359 (2003).

59. Yang, Y., Yu, W. W., Yan, W. & Xia, Q. Decorin induces cardiac hypertrophy by regulating the CaMKII/MEF-2 signaling pathway in vivo. *Curr. Med. Sci. 2021 415* **41**, 857–862 (2021).

60. Miska, E. A. et al. HDAC4 deacetylase associates with and represses the MEF2 transcription factor. *EMBO J.* **18**, 5099–5107 (1999).

61. Backs, J., Song, K., Bezprozvannaya, S., Chang, S. & Olson, E. N. CaM kinase II selectively signals to histone deacetylase four during cardiomyocyte hypertrophy. *J. Clin. Invest.* **116**, 1853 (2006).

62. Youn, H. D., Grozinger, C. M. & Liu, J. O. Calcium regulates transcriptional repression of myocyte enhancer factor 2 by histone deacetylase 4. *J. Biol. Chem.* **275**, 22563–22567 (2000).

63. Black, B. L. & Cripps, R. M. Myocyte enhancer factor 2 transcription factors in heart development and disease. *Hear. Dev. Regen.* 673–699. https://doi.org/10.1016/B978-0-12-381332-9.00030-X (2010).

64. Cornwell, J. D. & McDermott, J. C. MEF2 in cardiac hypertrophy in response to hypertension. *Trends Cardiovasc. Med.* https://doi.org/10.1016/J.TCM.2022.01.002 (2022).

65. Passier, R. et al. CaM kinase signaling induces cardiac hypertrophy and activates the MEF2 transcription factor in vivo. *J. Clin. Invest.* **105**, 1395 (2000).

66. Rodell, C. B. et al. Injectable shear-thinning hydrogels for minimally invasive delivery to infarcted myocardium to limit left ventricular remodeling. *Circ. Cardiovasc. Interv.* **9**, e004058 (2016).

67. Ifkovits, J. L. et al. Injectable hydrogel properties influence infarct expansion and extent of postinfarction left ventricular remodeling in an ovine model. *Proc. Natl Acad. Sci. USA* **107**, 11507–11512 (2010).

68. So, J. Y. et al. Regeneration of ischemic heart using hyaluronic acid-based injectable hydrogel. *J. Biomed. Mater. Res. Part B Appl. Biomater.* **91B**, 163–171 (2009).

69. Springer, M. L. et al. Localized arteriole formation directly adjacent to the site of VEGF-induced angiogenesis in muscle. *Mol. Ther.* **7**, 441–449 (2003).

70. Tous, E. et al. Influence of injectable hyaluronic acid hydrogel degradation behavior on infarction-induced ventricular remodeling. *Biomacromolecules* **12**, 4127–4135 (2011).

71. Chajara, A. et al. Increased hyaluronan and hyaluronidase production and hyaluronan degradation in injured aorta of insulin-resistant rats. *Arterioscler. Thromb. Vasc. Biol.* **20**, 1480–1487 (2000).

72. Chung, C., Beecham, M., Mauck, R. L. & Burdick, J. A. The influence of degradation characteristics of hyaluronic acid hydrogels on in vitro neocartilage formation by mesenchymal stem cells. *Biomaterials* **30**, 4287–4296 (2009).

73. Burdick, J. A. & Prestwich, G. D. Hyaluronic Acid Hydrogels for Biomedical Applications. *Adv. Mater.* **23**, H41–H56 (2011).

74. Dedkov, E. I. et al. Sex-related differences in intrinsic myocardial properties influence cardiac function in middle-aged rats with infarction-induced left ventricular remodeling. *Physiol. Rep.* **4**, e12822 (2016).

75. Dedkov, E. I., Oak, K., Christensen, L. P. & Tomanek, R. J. Coronary vessels and cardiac myocytes of middle-aged rats demonstrate regional sex-specific adaptation in response to postmyocardial infarction remodeling. *Biol. Sex. Differ.* **5**, 1–14 (2014).

76. Biondi-Zaccai, G. G. L. et al. Reduced post-infarction myocardial apoptosis in women: a clue to their different clinical course? *Heart* **91**, 99 (2005).